nature communications

Article

https://doi.org/10.1038/s41467-025-63975-1

Multilayered gradient $Ti_2AlC_{0.5}N_{0.5}$ prepared by crystal/amorphous C diffusion for efficient electromagnetic absorption and thermal shielding

Received: 26 November 2024

Accepted: 2 September 2025

Published online: 07 October 2025

Check for updates

Cheng Xie[1,2,3,5], Lei Xu[1,2,3] ✉, Zhigang Shen[4,5], Junyu Lu[1,2,3], Yongfen Sun[1,2,3], Zhaohui Han[1,2,3], Yuchen Feng[1,2,3] & Yanzhi Liu[1,2,3]

The unique advantages of surface/interface engineering are pivotal in advancing the design and development of high-performance electromagnetic wave (EMW) absorption materials. We present a universal microwave molten salt carbon (C) diffusion control strategy based on surface/interface engineering. This method leverages microwaves to promote the amorphous transformation and rapid diffusion of C on the carbon fiber surface, allowing for the rapid and controlled formation of three-dimensional multilayered gradient core-shell structures, primarily consisting of $Ti_2AlC_{0.5}N_{0.5}$ MAX. This unique structure with cavities contributes to the incident and multiple EMW losses. TACN-1 exhibited an efficient reflection loss of −83.4 dB at a thickness of just 1.9 mm and effectively isolates internal radiant heat, making it a promising material for stealth applications. This study not only advances the application of diffusion-controlled surface/interface engineering but also introduces a universal approach for modulating multilayered gradient structures in MAX phase ceramics.

The rapid advancements and widespread application of new-generation electronic information technologies have accelerated social progress and enhanced daily life convenience. However, the negative effects of long-term exposure to electromagnetic wave (EMW) radiation or pollution from increased use of electronic devices and their high-density use can cause interference with device functionality and potentially pose health risks. Developing EMW absorption materials is an effective way to reduce the amount of radiation that is reflected or transmitted, thus ensuring device functionality and potentially protecting human health[1–3]. There is a growing need for materials that can effectively absorb EMWs to protect against the radiation from the increased demand for smaller, complex wireless communication devices with wider operating frequencies. Consequently, this has spurred a significant push for the development of advanced EMW absorption materials, driving research into new materials, fabrication techniques, and application possibilities[4,5].

Traditional EMW absorbing materials, such as carbon-based materials[6], metal oxides[7], transition metal sulfides[8], metal-organic framework materials[9], and MAX phase ceramics[10], possess unique intrinsic properties related to their morphology, structure, electrical conductivity, dielectric properties, and impedance matching. However, while traditional EMW absorbing materials have their strengths,

[1]Faculty of Metallurgical and Energy Engineering, Kunming University of Science and Technology, Kunming, PR China. [2]National Local Joint Laboratory of Engineering Application of Microwave Energy and Equipment Technology, Kunming University of Science and Technology, Kunming, PR China. [3]The Key Laboratory of Unconventional Metallurgy, Ministry of Education, Kunming University of Science and Technology, Kunming, PR China. [4]SINOPEC Shanghai Research Institute of Petrochemical Technology CO. LTD, Shanghai, PR China. [5]These authors contributed equally: Cheng Xie, Zhigang Shen.
✉e-mail: xu_lei@kust.edu.cn; xulei_kmust@aliyun.com

single-phase absorption materials often fail to meet the advanced requirements of modern electronic technologies. Surface/interface engineering presents a valuable approach for enhancing the functionality of high-performance EMW absorption materials. By introducing multiple heterogeneous interfaces in EMW absorbers, their performance can be significantly enhanced by improving EMW loss and conversion efficiency[11–15]. MAX phase ceramics, a class of two-dimensional layered carbides or nitrides with tunable composition, exceptionally high-temperature resistance, and excellent electrical conductivity, have emerged as promising candidates for the design of high-performance EMW absorption materials[16–18]. Current research on MAX phase ceramics heavily focuses on the selective etching of the A-phase to produce MXenes, compositional modulation, and heterostructure construction[19–22]. MXenes extend the interlayer spacing, facilitating multiple EMW reflections, however, the surface of MXenes prepared by existing liquid-phase etching are rich in functional groups (–O, –OH, –F). The oxidation occurs slowly in air and rapidly in temperatures above 200 °C, their applicability becomes limited[23–25]. MAX phase ceramics with medium and high entropy were synthesized by adjusting the type and quantity of M-site metals, and a heterogeneous structure was developed by depositing magnetic metals and metal sulfides onto the surface of these ceramics to alter charge distribution and promote polarization loss. However, there are two limitations in using MAX phase ceramics: the dense structure between the layers of MAX phase ceramics and the limited study of their performance under varying temperatures. The dense structure hinders the creation of effective interfaces, weakening their EMW loss capabilities. Additionally, research primarily focuses on room temperature[22,26,27], leaving the impact of temperature on their EMW absorption performance unclear. The current report lacks a comprehensive approach to constructing a multiphase heterogeneous interface based on the structural design of MAX phase ceramics, optimizing its EMW absorption performance, and investigating the influence of temperature on its EMW absorption capabilities.

The molten salt method is a technique often used for synthesizing materials, particularly at high temperatures, where the molten salt acts as a reaction medium, it offers advantages like enhanced reactant diffusion, lower reaction temperatures, and the ability to control the final product's morphology[28,29]. As common salts, NaCl and KCl form a eutectic mixture with low melting points. This allows them to exist in a liquid state at relatively lower temperatures, which is advantageous in reactions. In addition, NaCl and KCl are widely used in molten salt synthesis due to their low cost, inert behavior in the molten state to prevent oxidation of materials, and ease of removal through dissolution and filtration[30–32].

In this study, we propose a C-diffusion synthesis strategy using a universal microwave molten salt approach, enabling the rapid and controlled preparation of a three-dimensional (3D) multilayered gradient structure, primarily composed of $Ti_2AlC_{0.5}N_{0.5}$ MAX (TACN), synthesized within 10 min through C-element diffusion control. The unique 3D multilayered gradient structure with cavities facilitates the incidence and multiple losses of EMW, whereas the abundant heterogeneous interfaces promote polarization loss. This results in effective polarization loss and efficient EMW absorption at the crystal/amorphous/crystal multiple interfaces. In addition, as EMW penetrates the outer ceramic layers, a substantial portion of the energy is absorbed by the inner amorphous/crystalline carbon fiber (CF), which efficiently converts the EMW into thermal energy. The multilayered gradient ceramics and cavity structure effectively isolate internal thermal radiation, enhancing the material's infrared shielding performance. This study elucidated the application of diffusion-controlled surface/interface engineering for the fabrication of 3D multilayered gradient core-shell structured EMW absorbers primarily composed of $Ti_2AlC_{0.5}N_{0.5}$, which provide exceptionally efficient EMW absorption and infrared heat shielding within 600 °C. It provides a simple yet effective strategy for the design and preparation of high-performance MAX phase ceramic.

Results and discussion

Mechanism of the preparation of a multilayered gradient MAX phase ceramic

In this work, a multilayered gradient TACN was successfully synthesized in 10 min using a microwave molten salt technique. Figure 1 depicts the fundamental mechanism of this process. Microwaves selectively heat materials based on their dielectric properties. This selective heating causes local overheating on the surface of the CF, while NaCl and KCl in the surrounding area melt quickly, creating a uniform liquid phase environment with strong polar force[30]. In the high-frequency alternating electromagnetic field generated by the microwave, the local high temperature and strong polar force of the molten salt facilitate CF amorphization and the rapid diffusion of C atoms. These atoms react with Ti in the molten salt, forming a TiC shell layer. Subsequently, under the influence of a reverse superheated temperature gradient and the Kirkendall effect, the C atoms are enabled to pass through the ceramic layer to further diffuse into the reaction system, reacting with Ti, Al, and AlN[33]. Within just 10 min, this process leads to the formation of a multilayered gradient core-shell structure predominantly composed of TACN. The unique multilayered gradient structure with cavities contributes to multiple incidences and EMW losses, enhancing the material's potential for EMW absorption applications[34].

Characterization of multilayered gradient MAX phase ceramic

The original CF had a smooth surface with a diameter of approximately 7.3 μm (Fig. 2a). As illustrated in Fig. 2b–d, the diameter of the TACN-1 increased to 11.4 μm, and its surface exhibited a rough texture resulting from the aggregation of numerous grains, with finer grain sizes observed on the inner surface. The diameter of TACN-2 increased with the increase in the reaction time, and the surface developed a layered structure on the surface (Supplementary Fig. 1a–c). In TACN-3, there was a reduction in surface porosity, and densification was more pronounced, revealing a clearer layered structure (Supplementary Fig. 1d–f). The sample size statistics are shown in Supplementary Fig. 2. The TACN samples predominantly exhibited lengths within the range of 40–140 μm (Supplementary Fig. 2a1, b1, c1), with 95% of TACN-1 samples falling between 7 μm and 15 μm, resulting in an average diameter of 11.3 μm (Supplementary Fig. 2a2). The average diameter of the TACN-2 samples increased to 12.6 μm, with 94% falling within the 9–17 μm range (Supplementary Fig. 2b2). The average diameter of the TACN-3 samples increased with the increase in reaction time to 14.3 μm, mainly distributed between 11 μm and 9 μm (Supplementary Fig. 2c2). The focused ion beam scanning electron microscope (FIB-SEM) was used to analyze the internal structure and elemental distribution of TANC-1, as shown in Fig. 1e, f. It revealed a core-shell structure with a cavity, exhibited a gradient distribution from the center to the periphery, illustrating the diffusion of C atoms driven by the Kirkendall effect. Ti, Al, and N elements were regionally enriched, contributing to the clear multilayered gradient structure in TACN-1. The C elements continued to diffuse outward with an increase in the reaction time, resulting in TACN-2 exhibiting a hollow tubular structure (Fig. 2g, h). In contrast, TACN-3 demonstrated a more uniform element distribution, lacking a multilayer gradient structure (Supplementary Fig. 3). The outer shell of TACN-1, as revealed by TEM images, is composed of grains stacked together with distinct grain boundaries (Supplementary Fig. 4a and 5a–c). This structure leads to an uneven distribution of electrons across the interface and promotes polarization at the grain boundaries. High-resolution transmission electron microscopy (HR-TEM) confirmed the presence of $TiC_{0.5}N_{0.5}$ in the inner layers and $Ti_2AlC_{0.5}N_{0.5}$ in the outer layers (Fig. 2i and Supplementary Fig. 4b, c), consistent with the SEM results for elemental

https://doi.org/10.1038/s41467-025-63975-1

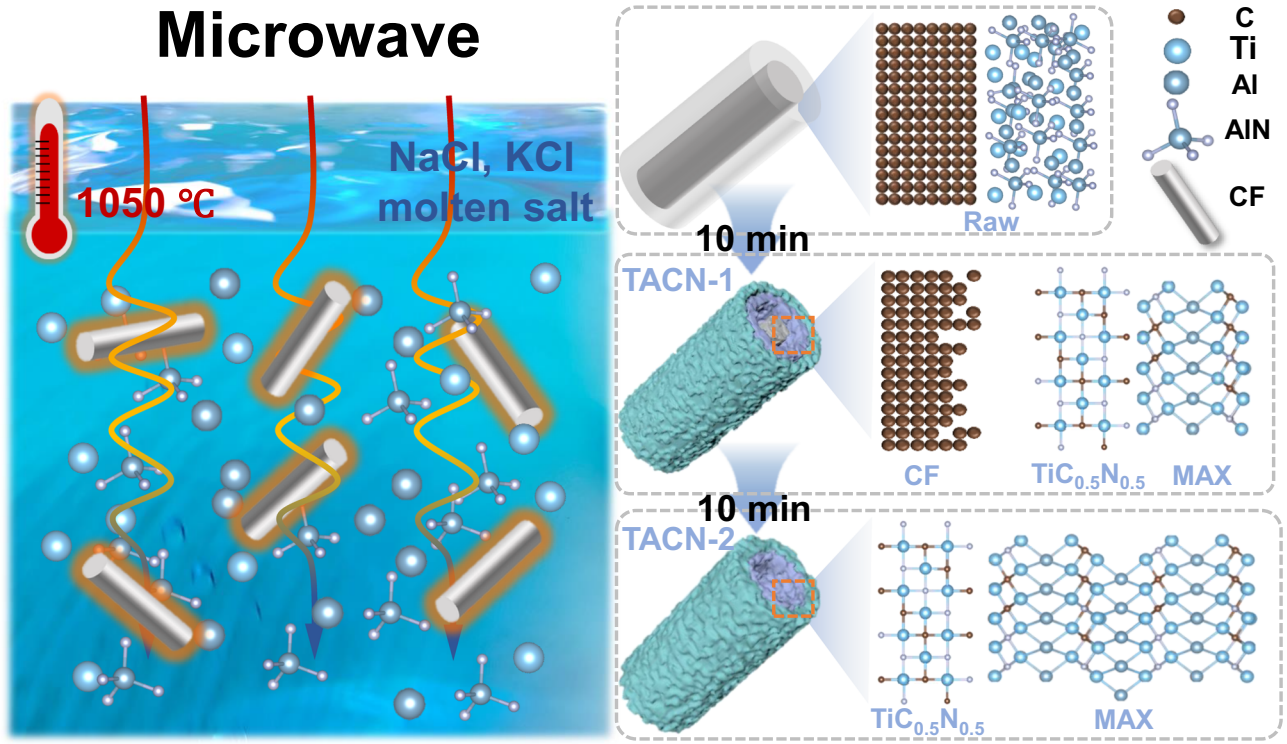

Fig. 1 | Schematic diagram of the preparation of a 3D multilayered gradient MAX phase ceramic. Three-dimensional multilayered gradient TACN phase ceramics were rapidly prepared using CF as raw materials by microwave molten salt technology.

distribution. Aberration-corrected transmission electron microscopy (AC-TEM) further analyzed the atomic arrangement and elemental distribution at the outer surface (Fig. 2j–l). The crystal plane distance of 0.68 nm corresponded to the (002) crystal plane of $Ti_2AlC_{0.5}N_{0.5}$ (JCPDS No.18-4884), confirming a typical 211-type MAX phase ceramic structure. Differences in the arrangement of Ti and Al atoms were observed, with Ti atoms appearing brighter and Al atoms darker. Ti and Al elements exhibited a layered distribution, whereas C and N were uniformly distributed between Ti (Fig. 2j–l, and Supplementary Fig. 6a, b). The rapid reaction resulted in numerous lattice defects and distortions within the shell (Supplementary Fig. 7a, b, d, e), which disrupted lattice symmetry and created a mismatch in lattice parameters, ultimately leading to an uneven distribution of stresses (Supplementary Fig. 7c, f). In addition, the gradient in elemental distribution also caused gradient changes in stress (Supplementary Fig. 8a, b). The lattice distortions, defects, and elemental gradients altered the electron distribution states and charge transfer pathways, leading to significant polarization effects[35]. TEM images of TACN-1 further revealed an irregular amorphous porous structure on the CF surface (Supplementary Fig. 9a, d) and a typical polycrystalline structure inside the CF (Supplementary Fig. 9e), which was characterized by the short-range ordering of the lattice and distinct crystal diffraction patterns[36]. These TEM results demonstrated that under localized high temperatures and molten salt etching, the CF underwent amorphization and diffused into the reaction system through the Kirkendall effect, forming pores on the surface and establishing an amorphous/crystalline interface. SEM, TEM, and AC-TEM results collectively revealed that TACN-1 exhibited a multilayered gradient structure, with a CF core and $TiC_{0.5}N_{0.5}/Ti_2AlC_{0.5}N_{0.5}$ shells. The ceramic shell contributed to the incidence of EMW, whereas the cavity between the core and shell promoted multiple reflections of the incident EMW. The phase gradient distribution, lattice defects in the ceramic shell, and the amorphous/crystalline interfaces within the CF contributed to changes in electron distribution states and charge transfer pathways. This enhanced interfacial polarization and improved the EMW absorption and loss capability of the samples.

X-ray diffraction (XRD) was used to determine the crystal phase composition of the samples (Fig. 3a). TACN-1 and TACN-2 exhibited the characteristic 211-type MAX phase ceramics and distinct diffraction peaks corresponding to $Ti_2AlC_{0.5}N_{0.5}$. As the reaction time increased, the MAX phase ceramics transitioned from type 211 to type 312 due to the ongoing diffusion of Ti and Al atoms, coupled with the reaction between $Ti_2AlC_{0.5}N_{0.5}$ and $TiC_{0.5}N_{0.5}$ at elevated temperatures (Fig. 3b)[37–39]. TACN-3 showed peaks characteristic of both 211-type and 312-type MAX phase ceramics (JCPDS No. 18-4884, 52-0875). Raman spectra showed a higher degree of disorder in TACN-1 (Fig. 3c), consistent with SEM, TEM, and AC-TEM results, showing that smaller grain sizes and lattice defects were present in the early stages of the reaction. Over time, smaller grains within a material grew larger and denser, resulting in a more ordered structure. In addition, the analysis of specific surface area also showed that the specific surface area gradually decreased with increased reaction time (Fig. 3d). The sample exhibited a type IV isotherm with H3 and H4 hysteresis loops, which corresponds to the irregular pore shapes due to grain accumulation. The BJH method revealed a dominant presence of mesopores within the sample (Supplementary Fig. 10). X-ray photoelectron spectroscopy (XPS) was used to examine the molecular structure and chemical state of the samples. In the high-resolution spectra of Ti 2*p* (Fig. 3e), characteristic peaks at 454.5 eV, 458.4 eV, and 460.7 eV were associated with Ti–C/N, Ti–Al, and Ti–N bonds, respectively. These peaks intensified with prolonged reaction time[40]. The Al 2*p* spectra (Supplementary Fig. 11a) showed increasing intensities for Al–Ti and Al–C/N at 71.6 eV and 74.2 eV, respectively. The C 1*s* spectrum (Supplementary Fig. 11b) displayed C–C and C–N bonds at 284.8 eV and 286.4 eV, whereas the N 1*s* spectrum (Supplementary Fig. 11c) revealed characteristic peaks of N–Ti and C=N at 396.4 eV and 399.4 eV. The N–Ti bond showed a gradual increase in intensity[41,42]. To further examine the atomic coordination environment of Ti, X-ray absorption fine

https://doi.org/10.1038/s41467-025-63975-1

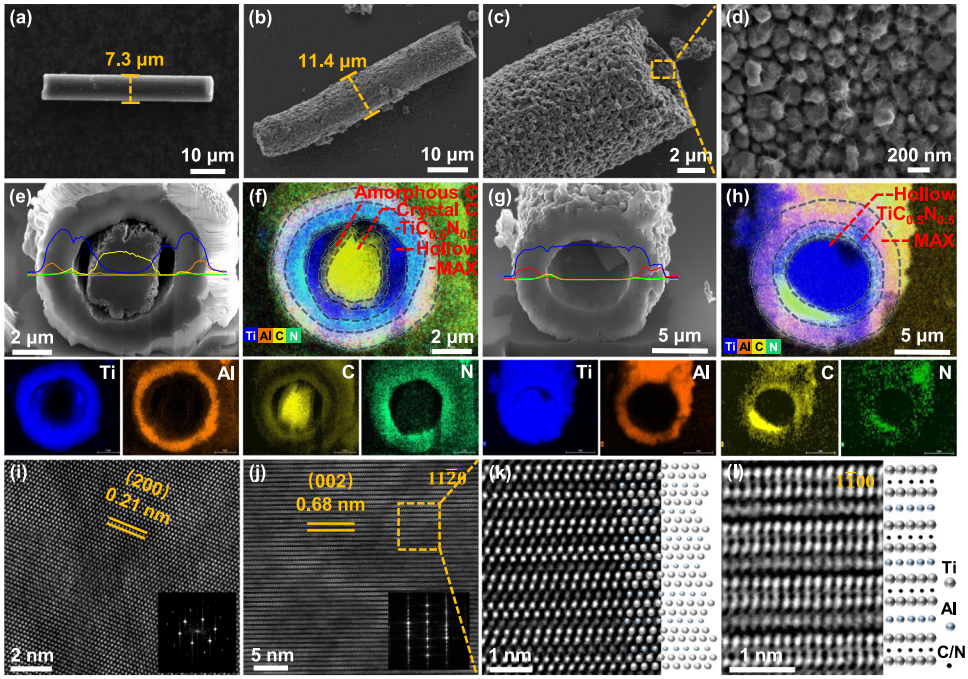

Fig. 2 | Microstructure of CF and TACN samples. SEM image of **a** CF and **b** TACN-1. SEM image of TACN-1 **c** outer surface and **d** inner surface. SEM images of cross-section and corresponding elemental distributions **e**, **f** TACN-1 and **g**, **h** TACN-2. HAADF-STEM image of TACN-1 **i** inner side of the shell and **j**, **k** surface. **l** iDPC-STEM image of the surface of TACN-1. The experiments were repeated three times independently with similar results.

structure (XAFS) analysis was performed. X-ray absorption near-edge spectra (XANES), as shown in Fig. 3f, showed that the valence states of Ti in TACN-1 were between 0 and +4. The Fourier transform of the k^3-weighted extended x-ray absorption fine structure (EXAFS) spectra (Fig. 3g) revealed strong scattering peaks at 1.5 and 2.4 Å, corresponding to Ti–C/N and Ti–Al bonds. To obtain more information about the atomic configuration of Ti in TACN-1, we carried out wavelet transform (WT)-EXAFS analysis. The contour plots of TACN-1 showed clear WT signals at 3.7 $Å^{-1}$ and 7.2 $Å^{-1}$, attributed to Ti–C/N and Ti-Al, respectively (Fig. 3h). The R-space fitting results indicated that the average bond lengths of Ti–C/N and Ti–Al were 2.1 Å and 2.86 Å, respectively (Fig. 3i, j and Supplementary Table 1)[43–45]. These results from XRD, XPS, and XAFS characterization confirm the successful synthesis of MAX phase transition metal carbon-nitride ceramics using the microwave molten salt C diffusion strategy, achieved within a short reaction time.

The electronic structure and bonding properties of TACN were further investigated by establishing a model based on microstructural characterization, as shown in Supplementary Fig. 12. Density functional theory (DFT) was employed to calculate the density of states (DOS) and partial density of states (PDOS) of $Ti_2AlC_{0.5}N_{0.5}$ (Supplementary Fig. 13). The results demonstrated that, in the MAX phase ceramic structure, the Ti atoms primarily formed bonds with the p-orbitals of Al, C, and N by using their d-orbitals. Moreover, the PDOS results for amorphous C and crystal C (Supplementary Fig. 14) showed that amorphous carbon exhibited a reduced DOS for conduction and lower electrical conductivity, which could mitigate the skinning effect on the surface of carbon-based materials.

To investigate the phase and structure transformations occurring under microwave molten salt conditions, XRD patterns of samples at varying reaction times were analyzed, as shown in Supplementary Fig. 15a. No clear MAX phase ceramic diffraction peaks were detected at 5 min; however, as time increased to 10–20 min, the 211-type MAX phase ceramics peaks were observed. 312-type characteristic diffraction peaks appeared at 30 min. Cross-sectional SEM images (Supplementary Fig. 15b–f, 16, and 17 and Fig. 2e, f) demonstrated a progressive increase in multilayered gradient structure ceramic layer thickness during the 5–15 min, with a gradual decrease in CF diameter, eventually forming a hollow tubular structure at 20 min. The thickness of the ceramic layer decreased with increasing densification. After 30 min, the ceramic layer had transformed into 312-type MAX phase ceramics, accompanied by a reduction in cavity size influenced by increased densification. Electron backscattered diffraction (EBSD) results revealed that the ceramic shell was composed of numerous grains with minor orientation differences, with grain sizes increasing as the reaction time increased (Supplementary Fig. 18). The inner grains were smaller, likely due to localized high temperature generated on the CF surface during the initial stages of the reaction under the microwave field. The large temperature gradient between the molten salt and the CF promoted rapid reactions and the generation of a large number of finer grains. The development of the ceramic shell impeded heat transfer as the reaction progressed, lowering the temperature gradient. Consequently, this reduced temperature gradient allows outer grains to continue growing into larger, more equiaxial crystals. The XRD, SEM, and EBSD results demonstrated that the ceramic shells formed under localized high temperatures and molten salts had smaller grain sizes and experienced rapid grain growth during the initial stages (0–10 min). After 10 min, the temperature gradient decreased, and the outer layer of the grains continued to grow and progressively became denser, gradually transforming from the 211 to the 312 MAX phase structure.

To further investigate the effect of microwave electromagnetic fields during the reaction process, CF was treated with microwave and conventional heated molten salt (NaCl and KCl). The XRD patterns of the treated CF (Supplementary Fig. 19a) revealed a significant reduction in the intensity of the (002) peaks after being treated with microwave-molten salt and conventional molten salt. Raman spectra (Supplementary Fig. 19b) demonstrated that the CF exhibited a higher degree of disorder following microwave molten salt treatment. The morphology of CF after conventional molten salt and microwave molten salt treatment is shown in Supplementary Fig. 19c, d. The groove structure on the surface of CF following microwave molten salt

https://doi.org/10.1038/s41467-025-63975-1

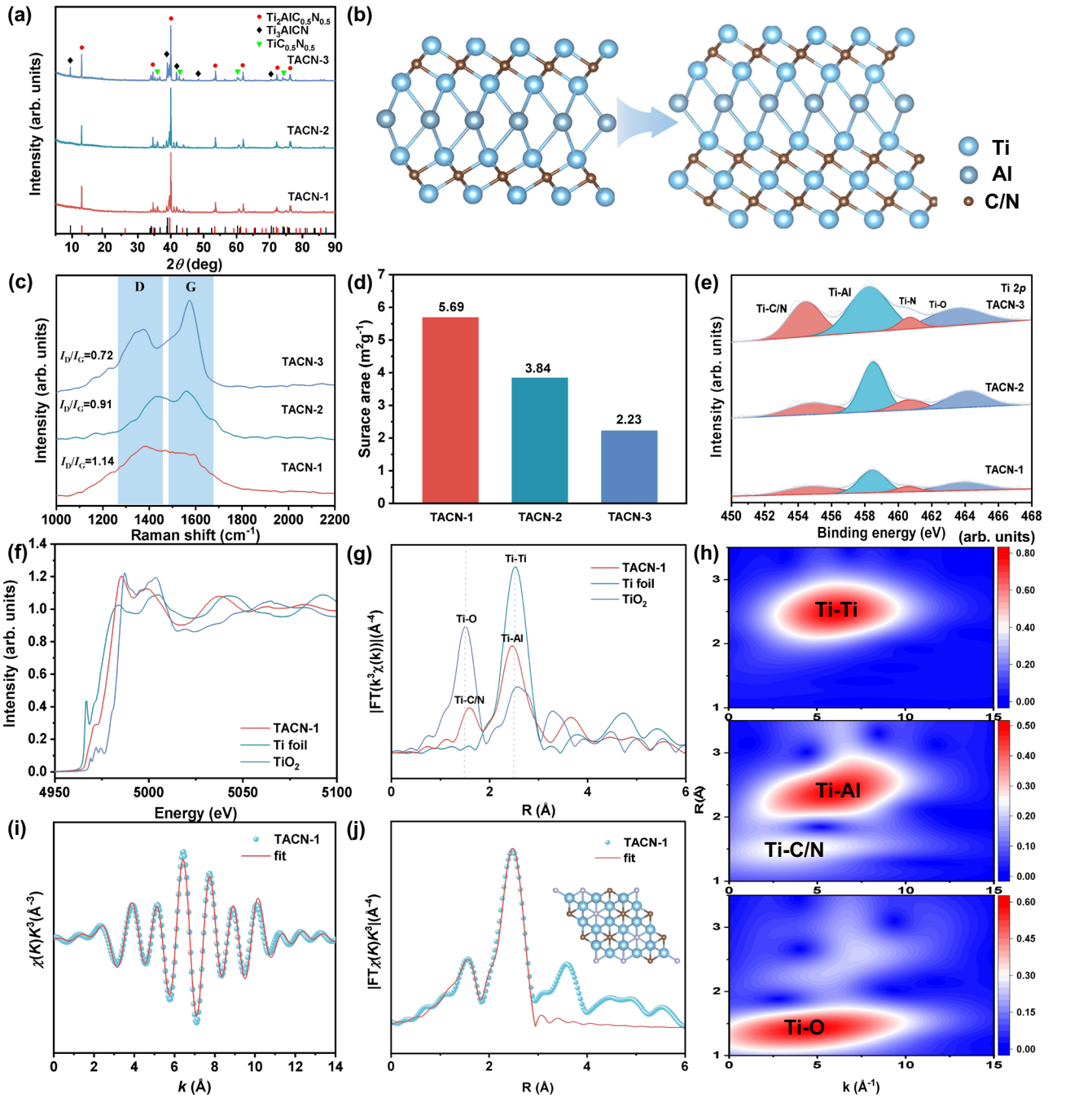

Fig. 3 | Characterization of the samples. a XRD pattern of samples, 211-type MAX (JCPDS no. 18-4884), 312-type MAX (JCPDS no. 52-0875). **b** Schematic of the phase transition of samples. **c** Raman spectra of samples. **d** Specific surface area of samples. **e** Ti 2*p* pattern of samples. **f** XANES spectra of TACN-1, Ti foil and TiO_2. **g** EXAFS spectra of TACN-1, Ti foil and TiO_2. **h** WT-EXAFS spectra of TACN-1, Ti foil and TiO_2. **i** k-space fitted to TACN-1. **j** R-space fitted for TACN-1. Source data are provided as a Source Data file.

treatment appeared more pronounced. After microwave molten salt treatment, the characteristic diffraction peaks of Ti powder decreased in intensity, while its morphology remained unchanged (Supplementary Fig. 20a–c). Similarly, no obvious phase and morphological changes were observed for AlN following microwave molten salt treatment (Supplementary Fig. 20d–f). The CF diameter significantly decreased following microwave molten salt treatment when Ti, Al, and AlN were added, and a rough, porous structure developed on the CF surface (Supplementary Fig. 21). CF, being an excellent microwave absorption carrier, generated localized high temperatures on its surface under the microwave field. These temperatures exceeded the surrounding molten salt environment. This temperature gradient is opposite to that of conventional heating. The synergistic effect of the microwave field and molten salt promoted the amorphous transformation of CF and its rapid diffusion into the system. In addition, the molten salt environment reduced the metal bonding energy[30], facilitating the reaction and enabling the rapid preparation of multilayer gradient TACN materials using microwave molten salt.

To assess the general applicability of the microwave molten salt C diffusion strategy, MAX phase ceramics with varying types and morphologies were prepared using different M/X ratios, C sources (spherical graphite, regenerated CF), and metals. As shown in Supplementary Fig. 22, the transitional phase (211-type) was the dominant physical phase over Ti_3AlCN in the early stage of the reaction (10 min),

but after 20 min, Ti_3AlCN became the dominant physical phase (Supplementary Fig. 22a). Ti_3AlCN-2 exhibited a hollow tubular structure and had an elemental distribution gradient (Supplementary Fig. 22a1–a3 and 23a). In addition, Spherical-$Ti_2AlC_{0.5}N_{0.5}$ and $V_2AlC_{0.5}N_{0.5}$ were efficiently synthesized using a microwave molten salt approach, exhibiting significant elemental distribution gradients (Supplementary Figs. 22b-b3, c-c3 and 23b, c). In addition, $Ti_2AlC_{0.5}N_{0.5}$ MAX phase ceramics were synthesized by conventional heating of molten salts and direct synthesis by microwave heating. The characterization results indicated that the conventional heating molten salt synthesis reaction proceeded slowly, exhibited a high level of impurity phases, and the morphology of the product directly synthesized by microwave was difficult to control (Supplementary Fig. 24 and 25). These experimental results showed that the microwave molten salt C diffusion strategy was versatile for the synthesis of multilayered gradient MAX phase ceramic materials. This method offers advantages such as high efficiency, rapid processing, and stable reactions, providing an effective route for synthesizing various MAX phase ceramic materials.

Electromagnetic performance of TACN samples

The electromagnetic parameters of the TACN samples were measured using a vector network analyzer (E5080B, Keysight, US) across a frequency range of 1–18 GHz (Fig. 4a–c). As shown in Supplementary Fig. 26a, the TACN samples showed fluctuating C_0 values at low frequencies, which converged into a straight line at high frequencies (Supplementary Eq. (1)). This behavior confirms that the samples exhibit natural resonance and interacting resonance properties, along with eddy current losses[46]. Magnetic property tests at room temperature indicated weak hysteresis in the TACN samples (Supplementary Fig. 26b). In addition, the μ′ and μ″ of the samples were close to 1 and 0, respectively (Fig. 4b), signifying that the contribution of magnetic loss to the attenuation and absorption of EMW in TACN was minimal. Therefore, the TACN's ability to absorb and dissipate EMW primarily arises from dielectric loss. To analyze the dielectric loss mechanism of TACN, the Cole–Cole curves were plotted based on Debye theory and Supplementary Eq. (2)[47], as shown in Supplementary Fig. 27. The Cole–Cole plots revealed long straight lines and multiple semicircles, corresponding to conduction loss (ε_c'') and polarization loss (ε_p''), respectively. Due to the excellent electrical conductivity of CF, which facilitates the generation of ε_c'', TACN-1 exhibited strong ε_c'', whereas TACN-2 showed a significantly weaker ε_c'' as a result of the reduced conductivity of the ceramic phase and the complete reaction of CF. In contrast, TACN-3 displayed enhanced ε_c'', attributed to the improved conductivity from the phase transition (Supplementary Fig. 28). The contributions of ε_c'' and ε_p'' to the dielectric loss in TACN were further analyzed. Specifically, the ε_c'' and ε_p'' of the samples were obtained using Debye's theory and Supplementary Eqs. (3–5) (Supplementary Fig. 29)[35]. The findings indicated that conduction loss was primarily observed in the frequency range of 1–4 GHz, with minor contributions, while polarization loss was the predominant factor affecting the dielectric loss in the 1–18 GHz range. Irregular semicircular curves were notably observed in the Cole–Cole curves of all the TACN samples (Supplementary Fig. 27), indicative of multiple polarization loss mechanisms. Lattice defects in the ceramic phase triggered dipole polarization under EMW, contributing to polarization loss. The grain boundaries, interfaces between $Ti_2AlC_{0.5}N_{0.5}$ and $TiC_{0.5}N_{0.5}$, interfaces between the ceramic phase and CF, the crystalline/amorphous interface in CF, and the rough sample surfaces impeded charge flow. This obstruction resulted in uneven electron distributions at these interfaces, which contributed to interfacial polarization. DFT calculations of the charge density difference at the interfaces in TACN-1 provided further insight into this phenomenon (Fig. 4d-f). At the $Ti_2AlC_{0.5}N_{0.5}/TiC_{0.5}N_{0.5}$ (Fig. 4d and Supplementary Fig. 30a) and $TiC_{0.5}N_{0.5}$/amorphous C (Fig. 4e and Supplementary Fig. 30b) interfaces, charge redistribution occurred. Similarly, as shown in Fig. 4f and Supplementary Fig. 30c, electrons were redistributed at the interfaces between amorphous C and crystal C, passing from crystal C to amorphous C. This spatially heterogeneous electron distribution promoted interfacial polarization, increasing the dissipation of EMWs. Moreover, the differences between the properties of C and N atoms in $Ti_2AlC_{0.5}N_{0.5}$, along with changes in bond lengths and bond angles in amorphous C, created a heterogeneous charge distribution that established localized electric fields and formed dipoles (Supplementary Fig. 31). These permanent dipoles oscillated within the electromagnetic field, amplifying dipole polarization loss. As a result, the polarization loss and the decay of EMW energy were further promoted.

EMW absorption performance of TACN samples

The EMW absorption performance of the TACN samples was evaluated using transmission line theory (Eqs. (1–2)). Among the samples, TACN-1 demonstrated superior EMW absorption properties (Fig. 4g, h and Supplementary Fig. 32), achieving a minimum reflection loss (RL_{min}) of -83.4 dB in the X-band at a thickness of 1.9 mm, along with a maximum effective absorption bandwidth (EAB) of 3.4 GHz at a thickness of 1.2 mm. In contrast, TACN-2 reached −50.0 dB at the same thickness of 1.9 mm, with a maximum EAB of 3.8 GHz at 1.3 mm. TACN-3 achieved −69.6 dB in the Ku-band with a maximum EAB of 3.8 GHz at 1.3 mm, and the RL_{min} of TACN-3 reached −69.6 dB in the Ku-band. The EMW absorption performance of TACN-0.5 and TACN-1.5 in the Ku-band is presented in Supplementary Fig. 33, with an RL_{min} of −62.7 dB for both. In addition, the synthesized Ti_3AlCN MAX phase ceramics also exhibited significant EMW absorption capacity (Supplementary Fig. 34), whereas $V_2AlC_{0.5}N_{0.5}$ failed to show a competitive level of EMW absorption capacity (Supplementary Fig. 35). Generally, for optimal EMW absorption performance, the materials should have an optimal impedance match (Z), where the normalized input impedance ($|Z_{in}/Z_0|$) was selected to characterize the impedance (Supplementary Eq. (6))[48]. When the value of $|Z_{in}/Z_0|$ falls between 0.8 and 1.2, it generally indicates optimal impedance matching. CF exhibited high electrical conductivity; however, factors such as the skin effect can cause worse impedance matching and EMW absorption performance (Supplementary Fig. 36 and 37). Amorphization on the CF surface reduces the conductivity and improves the EMW absorption performance (Supplementary Fig. 38). The construction of the surface multilayered gradient ceramic structure enabled TACN-1 to exhibit better impedance matching performance. As the structure changed and phase transformation occurred, the $|Z_{in}/Z_0|$ values for TACN-2 and TACN-3 increased, resulting in more significant impedance mismatches (Fig. 4h, i and Supplementary Fig. 32a1–c2). In addition, the multilayered gradient structure and high α value of TACN-1 facilitated efficient EMW penetration, loss, and conversion (Supplementary Fig. 39), further enhancing its absorption performance. Compared to other MAX phase ceramics and various EMW absorbers, TACN exhibited excellent EMW absorption properties (Supplementary Fig. 40 and Supplementary Table 2). In addition, the effect of temperature on the EMW absorption performance of the samples was also investigated. The thermogravimetric results showed that the mass change of the samples remained relatively insignificant within 600 °C (Supplementary Fig. 41a–c). The electromagnetic parameters of the TACN samples at various temperatures were obtained using the resonant cavity perturbation method at a frequency of 2.45 GHz, as shown in Supplementary Fig. 41d–f. It was observed that the electromagnetic parameters of the samples remained largely stable within the temperature range of 50–600 °C. It was demonstrated that the TACN samples exhibit stable and efficient absorption of EMWs across a temperature range from room temperature to 600 °C.

To simulate real-world applications, a 3D radar cross-section (RCS) simulation of TACN was performed using CST Studio to simulate the EMW absorption performance of the materials. The simulation

https://doi.org/10.1038/s41467-025-63975-1

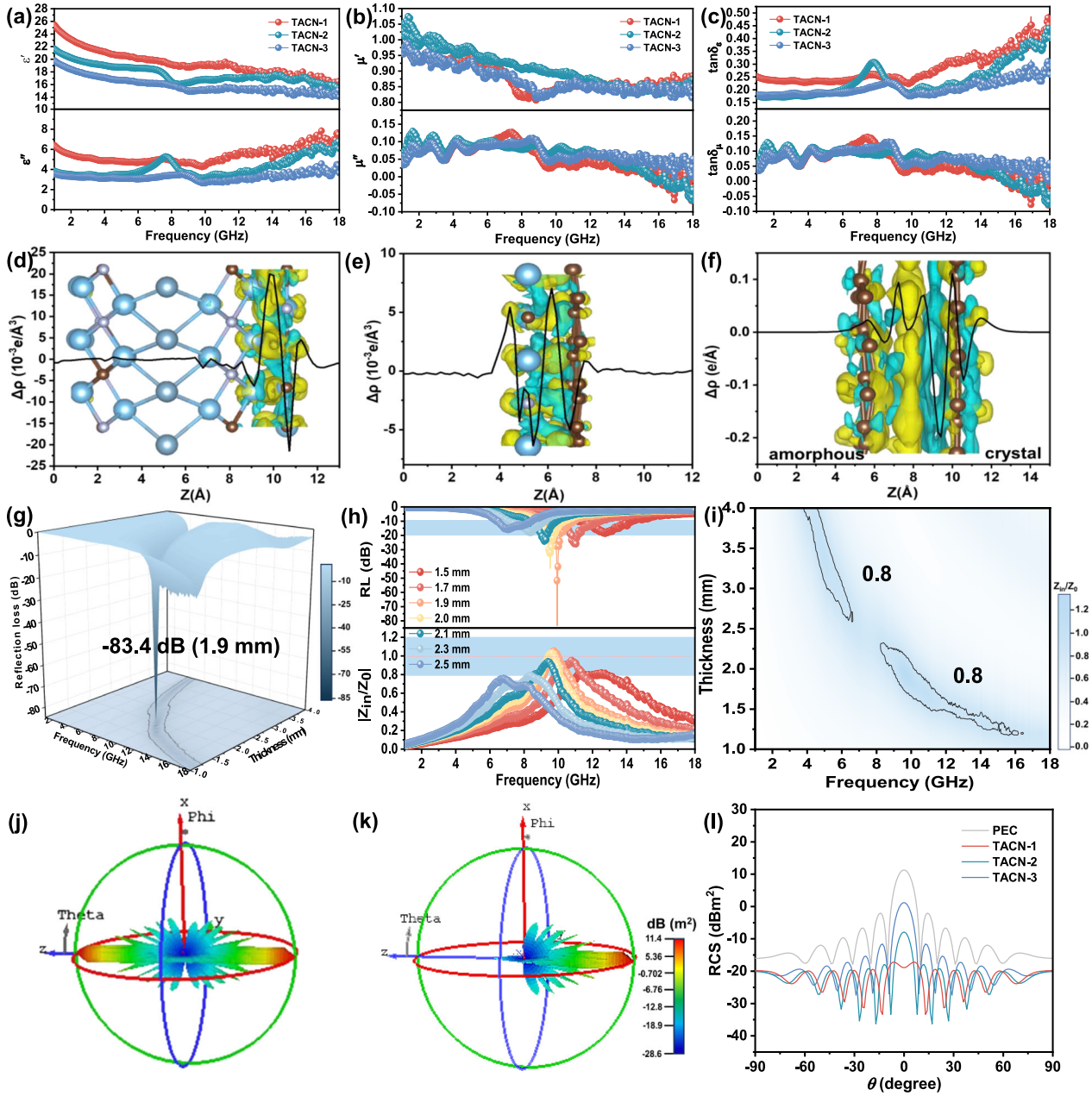

Fig. 4 | EMW absorption properties of samples. a–c The electromagnetic parameters of TACN-1, TACN-2, and TACN-3. **d** Interfacial charge density difference of $Ti_2AlC_{0.5}N_{0.5}/TiC_{0.5}N_{0.5}$. **e** Interfacial charge density difference of $TiC_{0.5}N_{0.5}$/amorphous C. **f** Interfacial charge density difference of Amorphous C/crystal C. **g–i** Reflection loss and impedance matching of TACN-1. **j** RCS simulation result of a PEC. **k** RCS simulation result of TACN-1. **l** 2D RCS reflection curves of PEC, TACN-1, TACN-2, and TACN-3. Source data are provided as a Source Data file. The experiments were repeated three times independently with similar results.

model consisted of TACN and a perfect conductor (PEC) (Supplementary Fig. 42a). The reflected signal intensity from the pure PEC plate and TACN coating was monitored under vertically incident EMW across the entire detection angle, with a thickness of 1.9 mm and a frequency of 9.9 GHz. As shown in Fig. 4j, k and Supplementary Fig. 42b, c, the PEC reflected all the incident EMW, whereas TACN-1 exhibited the lowest 3D RCS reflection intensity, which was significantly lower than that of TACN-2, TACN-3, and the PEC. In particular, TACN-1 maintained an RCS value below −15 dBm^2 across a wide angular range from −90° to 90° (Fig. 4l). At θ = 0°, the RCS was reduced by 30.2 dBm^2 compared to the pure PEC (Supplementary Fig. 42d). These results demonstrate that TACN-1 exhibits excellent EMW attenuation performance, effectively minimizing the scattering and reflection of EMW on the PEC surface.

Infrared heat shielding performance of TACN samples

To evaluate the EMW conversion loss and practical application potential of TACN, infrared thermography was used to monitor the temperature changes of CF and TACN samples under a 2.45 GHz microwave electromagnetic field. The ceramic properties and multilayered gradient structure of the TACN samples significantly reduced their thermal conductivity (Fig. 5a). As shown in Fig. 5b, c, under 300 W microwave power, the surface temperature of CF increased rapidly from room temperature to 199.7 °C within 10 s. In contrast, the surface temperature of TACN-1, with its ceramic shell, was only 60 °C at 10 s, gradually rising to 98.3 °C after 100 s. TACN-2, composed of a pure ceramic structure, had an even lower temperature of 50 °C after 100 s of microwave heating. The heating and cooling curves (Fig. 5b and Supplementary Fig. 43) showed that CF

https://doi.org/10.1038/s41467-025-63975-1

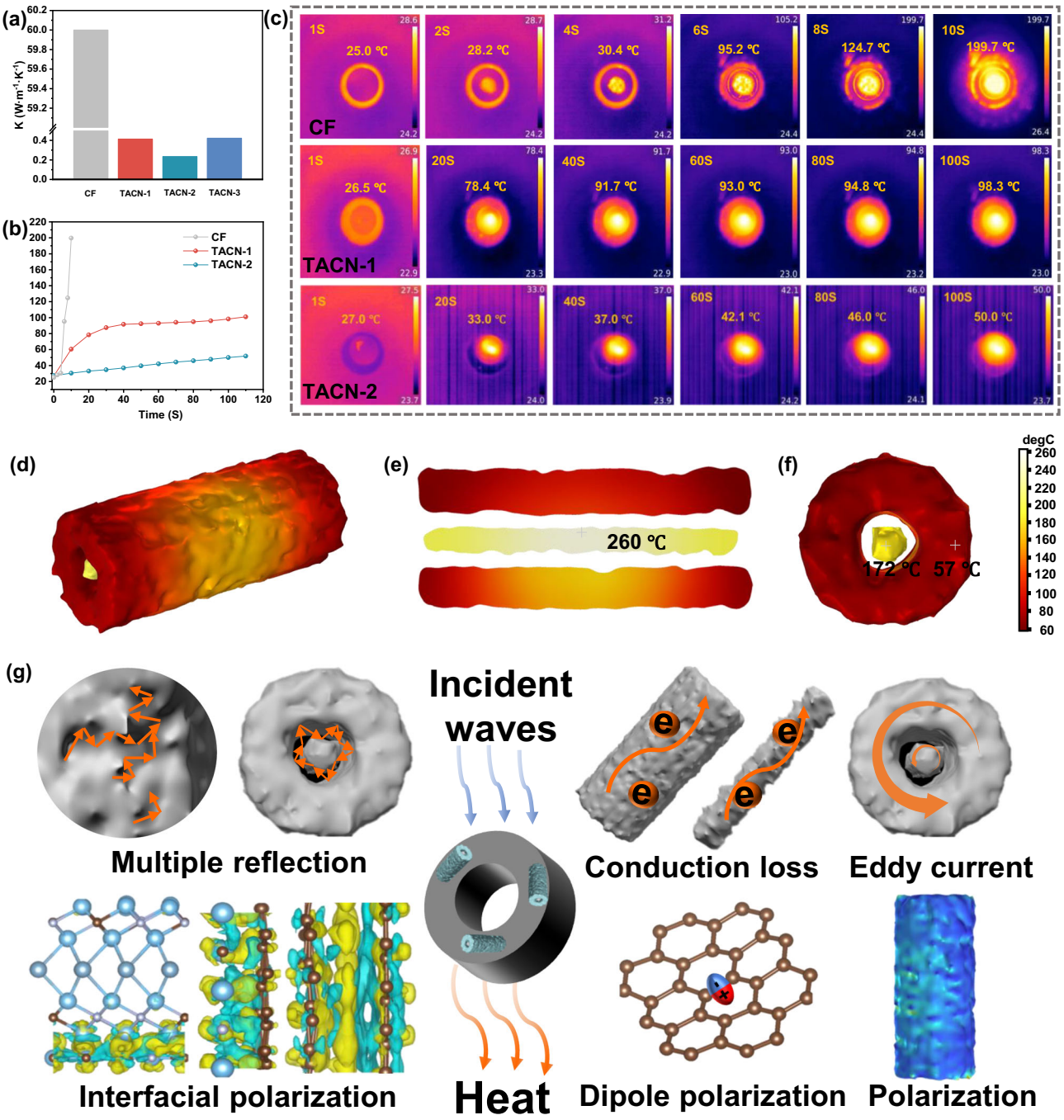

Fig. 5 | Infrared heat shielding performance and schematic of EMW absorption of TACN samples. a Thermal conductivity of CF, TACN-1, and TACN-2. **b** Heating curves of CF, TACN-1, and TACN-2 under the microwave. **c** Infrared thermography pictures of CF, TACN-1, and TACN-2 under the microwave. **d**–**f** COMSOL temperature field simulation results of TACN-1. **g** EMW absorption mechanism of TACN-1. Source data are provided as a Source Data file.

heats up and cools down faster because of its higher thermal conductivity. In contrast, the multilayered gradient ceramic shells and cavities of TACN-1 served as thermal insulators, lowering surface temperatures and slowing down heating and cooling rates. COMSOL was used to investigate the heating behavior of the samples under 2.45 GHz and 300 W microwave power. A model with a CF core and ceramic shell was created (Supplementary Fig. 44a–c). The temperature distributions after 10 s of microwave exposure are shown in Fig. 5d. The cross-sectional temperature fields (Fig. 5e, f) showed that the center of the CF reached the highest temperature of 260 °C, whereas the ends were 172 °C. The temperature at the ends of the ceramic shell was only 57 °C, significantly lower than that of the CF. Furthermore, the electric field results showed (Supplementary Fig. 44d–f) a significant heterogeneous polarization effect on the surface of the ceramic shell and CF. Both experimental and simulation results confirmed that TACN-1 achieves efficient EMW attenuation primarily through multiple polarization loss mechanisms. As EMW penetrates the outer ceramic layer, a substantial portion of EMW is absorbed by the internal amorphous/crystal CF, converting it into heat. The multilayered gradient core-shell structure and cavities of the outer layer, primarily composed of $Ti_2AlC_{0.5}N_{0.5}$ MAX, offer efficient insulation by protecting against internal radiant heat and reducing infrared thermal image detection, highlighting its potential use in stealth material applications[49].

Based on these results, we demonstrated that designing and constructing a multilayered gradient structure was an effective strategy for realizing efficient EMW absorption and loss in MAX phase ceramic materials. As illustrated in Fig. 5g, the 3D multilayered gradient structure could effectively increase the EMW scattering area while reducing material density (Supplementary Fig. 45). The ceramic shell and CF form a conductive network that promotes electron migration and eddy current loss[50–52]. Moreover, the crystal/amorphous/crystalline multiple interfaces and the rough surfaces of the samples create heterogeneous distributions of interfacial charges, leading to interfacial polarization[53–55]. The differing properties of C and N, combined with defects in the ceramic shell and the irregular structure of amorphous carbon, result in dipole polarization[56,57], thus enabling polarization loss and highly efficient EMW absorption at the crystal/amorphous/crystalline multiple interfaces.

In summary, this work introduced a universal microwave molten salt C diffusion-controlled synthesis strategy that leverages surface/interface engineering. This method enhances the amorphous transformation and C diffusion on the surfaces of carbon materials by leveraging the synergistic effect of a microwave field and molten salt. By manipulating reaction conditions, the morphology and multilayered gradient structure of the materials can be effectively controlled, enabling the rapid synthesis of MAX ceramic materials with a 3D multilayered gradient structure. The unique 3D multilayered gradient structure and the presence of cavities enhance the attenuation of EMW through incident and multiple reflections. The rich heterogeneous interfaces promote interfacial polarization, leading to multiple attenuation and loss of EMW. TACN-1 demonstrated excellent EMW absorption performance, achieving an RL_{min} of −83.4 dB at a thickness of 1.9 mm. Moreover, the multilayered gradient ceramics with cavities offer promising solutions for internal radiation heat isolation, potentially leading to lower surface temperatures and enhanced stealth applications. This study presents a microwave molten salt C diffusion synthesis strategy that successfully enables the efficient synthesis of 3D multilayered gradient-structured MAX phase ceramic materials, offering both highly efficient EMW absorption and infrared heat shielding within 600 °C. This approach broadens the pathways for material synthesis and offers a fresh perspective for designing and developing functional materials.

Methods

Materials: Titanium powder (Ti, 98%), vanadium powder (V, 99.5%), aluminum powder (Al, ≥99%), aluminum nitride (AlN, ≥99%), sodium chloride (NaCl, ≥99%), potassium chloride (KCl, ≥99%), anhydrous ethanol (C_2H_5OH, ≥99.9%), and the reagents were all purchased from Macklin. CF (length: 0.5 mm) and spherical graphite (diameter: 8 μm) were purchased from Yunnan Yidun Biotechnology Co., Ltd., and the regenerated carbon fiber (rCF, length: 0.5 mm) was recovered by pyrolysis of discarded CF composite sheets and then sheared. The water used in the experimental process was all deionized water.

TACN Preparation: Ti, Al, AlN, CF, NaCl, KCl to the molar ratio of 2:0.5:0.5:0.5:4:4 placed in a mortar grinding mixture, the mixture was transferred to a crucible, placed in a microwave high-temperature atmosphere sintering furnace, microwave irradiation at 1050 °C to maintain 5 min, 10 min, 15 min, 20 min, 30 min. After the reaction was completed, the mixture was naturally cooled to room temperature, and the reacted mixture was washed with deionized water to remove NaCl and KCl, and washed and filtered to obtain the black precipitate, which was put into the blast drying oven to dry at 60 °C for 12 h, and then grinded through a 400-mesh sieve to obtain the used TACN-0.5, TACN-1, TACN-1.5, TACN-2, and TACN-3 (Among them, 0.5, 1, 1.5, 2 and 3 correspond to the reaction time of 5 min, 10 min, 15 min, 20 min and 30 min, respectively).

Ti_3AlCN preparation: Ti, AlN, rCF, NaCl, KCl to the molar ratio of 3:1:1:4:4 placed in the mortar grinding mixture, the mixture was transferred to the crucible, put into the microwave high temperature atmosphere sintering furnace microwave irradiation 1150 °C to maintain 10 min, 20 min, 30 min, after the completion of the reaction, the reaction is naturally cooled to room temperature, the reaction mixture was washed with deionized water to remove NaCl and KCl, washed and filtered to obtain black precipitate, put into the blast drying oven at 60 °C for 12 h, and then grinded through a 400-mesh sieve to obtain the used Ti_3AlCN-1, Ti_3AlCN-2 and Ti_3AlCN-3 (Among them, 1, 2 and 3 correspond to the reaction time of 10 min, 20 min and 30 min, respectively).

Spherical-$Ti_2AlC_{0.5}N_{0.5}$ preparation: Ti, Al, AlN, spherical C, NaCl, KCl to molar ratio of 2:0.5:0.5:0.5:4:4 placed in a mortar grinding mixture, the mixture was transferred to the crucible, placed into the microwave high-temperature atmosphere sintering furnace microwave irradiation 1050 °C to maintain the 10 min, 20 min, 30 min, after the reaction is completed After the reaction was completed, the mixture was naturally cooled to room temperature, the reaction was washed with deionized water to remove NaCl, KCl, washed and filtered to obtain the black precipitate, put into the blast drying oven at 60 °C for 12 h, grinding over 400 mesh sieve to obtain the used S-$Ti_2AlC_{0.5}N_{0.5}$-1, S-$Ti_2AlC_{0.5}N_{0.5}$-2, S-$Ti_2AlC_{0.5}N_{0.5}$-3 (Among them, 1, 2 and 3 correspond to the reaction time of 10 min, 20 min and 30 min, respectively).

$V_2AlC_{0.5}N_{0.5}$ Preparation: V, Al, AlN, CF, NaCl, KCl to the molar ratio of 2:0.5:0.5:0.5:4:4 placed in a mortar grinding mixture, the mixture was transferred to the crucible, placed into the microwave high-temperature atmosphere sintering furnace microwave irradiation 1050 °C to keep 10 min, 20 min, 30 min, after the reaction is completed, natural cooling to After the reaction was completed, the reaction mixture was washed with deionized water to remove NaCl, KCl, washed and filtered to obtain the black precipitate, put into the blast drying oven at 60 °C for 12 h, grinding through 400 mesh sieve to obtain the used $V_2AlC_{0.5}N_{0.5}$-1, $V_2AlC_{0.5}N_{0.5}$-2, $V_2AlC_{0.5}N_{0.5}$-3 (among them, 1, 2 and 3 correspond to the reaction time of 10 min, 20 min and 30 min, respectively).

Characterization: The crystal structure of the samples was characterized by XRD (X Pert PRO MPD, PANalytical, Netherlands, Cu Ka). The SEM (SU8030, HITACHI, Japan), HRTEM (TecnaiG2 TF30, FEI, US), and AC-STEM (Theims Z, FEI, US) were employed to analyze the microstructure and morphology. XPS (Thermo Fisher Scientific, UK) was performed to analyze the chemical states of elements. Ti **K**-edge analysis was performed with Si (111) crystal monochromators at the BL14W1 beamlines at the Shanghai Synchrotron Radiation Facility (SSRF) (Shanghai, China). The DC conductivity (σ) of the concentric rings shape sample measurements was performed by a semiconductor analyzer (4200A-SCS, Keithley, US). The thermal conductivity of the samples was tested by a laser thermal conductivity meter (LFA 467HT Hyperflash, Netzsch, Germany). A vector network analyzer (E5080B, Keysight, US) was used to record the electromagnetic parameters (complex permittivity ($\varepsilon_r = \varepsilon' - j\varepsilon''$) and permeability ($\mu_r = \mu' - j\mu''$) by a typical coaxial-line method in the frequency range from 1 GHz to 18 GHz. Before detection, all samples (50 wt%) were compressed into coaxial rings (Φ_{in} = 3.04 mm, Φ_{out} = 7.00 mm) in paraffin. Accordingly, based on the transmission line theory, the EMW absorption performance and reflection loss (RL) values were given by the following equations:

$$RL = 20\log_{10}\frac{|Z_{in} - Z_0|}{|Z_{in} + Z_0|} \quad (1)$$

$$Z_{in} = Z_0\sqrt{\mu_r/\varepsilon_r}\tanh\left[j(2\pi f d/c)\times\sqrt{\mu_r\varepsilon_r}\right] \quad (2)$$

where Z_0, Z_{in}, d, f, and c represent the impedance in free space, the input impedance of the absorber, the thickness of the absorber, and the frequency and velocity of EMW of light in vacuum, respectively.

DFT: All the calculations are performed in the framework of the DFT with the projector augmented plane-wave method, as implemented in the Vienna ab initio simulation package[58]. The generalized gradient approximation proposed by Perdew–Burke–Ernzerhof (PBE) is selected for the exchange-correlation potential[59]. The cut-off energy for the plane wave is set to 480 eV. The energy criterion is set to 10^{-4} eV in the iterative solution of the Kohn-Sham equation. All the structures are relaxed until the residual forces on the atoms have declined to less than 0.02 eV/Å. To avoid interlaminar interactions, a vacuum spacing of 20 Å is applied perpendicular to the slab.

Here, we define $\Delta\rho = \rho_{A-B} - \rho_A - \rho_B$ as the charge density difference of A/B heterostructure, where ρ_{A-B}, ρ_A and ρ_B are the charge densities of A/B heterostructure, isolated A and B slabs, respectively.

Reporting summary

Further information on research design is available in the Nature Portfolio Reporting Summary linked to this article.

Data availability

The data generated in this study are provided in the Supplementary Information/Source Data file. Source data are provided with this paper.

References

1. Iqbal, A. et al. Anomalous absorption of electromagnetic waves by 2D transition metal carbonitride Ti_3CNT_x (MXene). *Science* **369**, 446–450 (2020).
2. Zhao, R. et al. Highly anisotropic Fe_3C microflakes constructed by solid-state phase transformation for efficient microwave absorption. *Nat. Commun.* **15**, 1497 (2024).
3. Hou, Y. et al. Hygroscopic holey graphene aerogel fibers enable highly efficient moisture capture, heat allocation and microwave absorption. *Nat. Commun.* **13**, 1227 (2022).
4. Qu, N. et al. 2D/2D coupled MOF/Fe composite metamaterials enable robust ultra–broadband microwave absorption. *Nat. Commun.* **15**, 5624 (2024).
5. Cheng, Y. et al. Hierarchically porous polyimide/$Ti_3C_2T_x$ film with stable electromagnetic interference shielding after resisting harsh conditions. *Sci. Adv.* **7**, 1663 (2021).
6. Wu, F. et al. Multifunctional carbon Fiber@TiO_2/C aerogels derived from MXene for pressure tunable microwave absorption. *Carbon* **230**, 119644 (2024).
7. Cheng, Z. et al. Intelligent off/on switchable microwave absorption performance of reduced graphene oxide/VO_2 composite aerogel. *Adv. Funct. Mater.* **32**, 2205160 (2022).
8. Wang, J. et al. Controllable regulation of MoS_2 surface atomic exposure for boosting interfacial polarization and microwave absorption. *Adv. Funct. Mater.* **34**, 2409923 (2024).
9. Ma, X. et al. Bridging dielectric-magnetic synergistic units with MOFs on fibers structure for high-efficient microwave absorption at low filler loading. *Carbon* **229**, 119444 (2024).
10. Liu, Y. et al. Lewis acid molten salt etched porous lamellar Ti_2AlC powders for enhanced microwave absorption. *Ceram. Int.* **50**, 8546–8550 (2024).
11. Li, S. et al. Lightweight Fe_3O_4/Fe/C/rGO multifunctional aerogel for efficient microwave absorption, electromagnetic interference shielding, hydrophobicity and thermal insulation. *Chem. Eng. J.* **498**, 155405 (2024).
12. Wang, J. et al. Hierarchical carbon fiber@MXene@MoS_2 core-sheath synergistic microstructure for tunable and efficient microwave absorption. *Adv. Funct. Mater.* **30**, 2002595 (2020).
13. Liu, X. et al. Heterointerface-engineered SnO_2@SnO nanoparticle@foamed C composites for prominent microwave absorption and thermal conduction performance. *Chem. Eng. J.* **497**, 154492 (2024).
14. Shi, X. et al. Interface engineering in the hierarchical assembly of carbon-confined Fe_3O_4 nanospheres for enhanced microwave absorption. *J. Mater. Chem. A* **10**, 8807 (2022).
15. Liu, X. et al. Morphology- and defect-coordinated prominent microwave absorption, thermal exhaustion, and electrical insulation in SnO_2@SnP_2O_7@$Sn_2P_2O_7$ hierarchical architectures. *J. Mater. Chem. A* **12**, 12452 (2024).
16. Fu, Z. et al. Rational design of flexible two-dimensional MXenes with multiple functionalities. *Chem. Rev.* **119**, 11980–12031 (2019).
17. Zhou, J. et al. Atomic scale design of mxenes and their parent materials-from theoretical and experimental perspectives. *Chem. Rev.* **123**, 13291–13322 (2023).
18. Shao, H. et al. Synthesis of MAX phase nanofibers and nanoflakes and the resulting MXenes. *Adv. Sci.* **10**, 2205509 (2023).
19. Shahzad, F. et al. Electromagnetic interference shielding with 2D transition metal carbides (MXenes). *Science* **353**, 1137–1140 (2016).
20. Wan, S. et al. High-strength scalable MXene films through bridging-induced densification. *Science* **374**, 96–99 (2021).
21. Bai, X. et al. Magnetic-dielectric synergistic construction of Ni-doped Ti_3AlC_2 achieving efficient microwave absorption. *Ceram. Int.* **49**, 40570–40580 (2023).
22. Han, J. et al. Anomalous electromagnetic wave absorption of MAX phase ceramic powder achieved through high entropy solid solution and melt pool heat transfer preparation method. *J. Mater. Sci. Mater. Electron* **35**, 883 (2024).
23. Kim, J. et al. Chemically stabilized and functionalized 2D-MXene with deep eutectic solvents as versatile dispersion medium. *Adv. Funct. Mater.* **31**, 2008722 (2021).
24. Soomro, R. et al. Progression in the oxidation stability of MXenes. *Nanomicro Lett.* **15**, 108 (2023).
25. Lee, Y. et al. Oxidation-resistant titanium carbide MXene films. *J. Mater. Chem. A* **8**, 573 (2020).
26. Zhang, Z. et al. Synthesis and electromagnetic wave properties of $Ti_{2.7}M_{0.1}T_{0.2}AlC_2$ (M = Fe, Ni, T = Zr, Mo, W, Ta) powder. *J. Alloy. Compd.* **978**, 173472 (2024).
27. Chen, L. et al. Multiprincipal element M_2FeC (M = Ti, V, Nb, Ta, Zr) MAX phases with synergistic effect of dielectric and magnetic loss. *Adv. Sci.* **10**, 2206877 (2023).
28. Liu, X. et al. Salt melt synthesis of ceramics, semiconductors and carbon nanostructures. *Chem. Soc. Rev.* **42**, 8237 (2013).
29. Roy, C. et al. Molten salt shielded synthesis (MS^3) of Ti_2AlN and V_2AlC MAX phase powders in open air. *J. Eur. Ceram. Soc.* **40**, 923–929 (2020).
30. Chen, D. et al. Molten salt-assisted synthesis of catalysts for energy conversion. *Adv. Mater.* **36**, 2408285 (2024).
31. Li, M. et al. Preparation of TiC/Ti_2AlC coating on carbon fiber and investigation of the oxidation resistance properties. *J. Am. Ceram. Soc.* **101**, 5269–5280 (2018).
32. Khan, M. et al. Factors influencing synthesis and properties of MAX phases. *Sci. China Mater.* **67**, 3427–3455 (2024).
33. Yin, Y. et al. Formation of hollow nanocrystals through the nanoscale kirkendall effect. *Science* **304**, 711–714 (2004).
34. Wu, Z. et al. Dimensional design and core–shell engineering of nanomaterials for electromagnetic wave absorption. *Adv. Mater.* **34**, 2107538 (2022).
35. Tang, Z. et al. Synthesis of $CuCo_2S_4$@expanded graphite with crystal/amorphous heterointerface and defects for electromagnetic wave absorption. *Nat. Commun.* **14**, 5951 (2023).
36. Ren, Y. et al. Study on oxidation behavior during process of recycling carbon fibers from CFRP by pyrolysis. *J. Environ. Manag.* **347**, 119103 (2023).
37. Zhong, Y. et al. Molten salt synthesis and formation mechanism of Ti_3AlC_2: a new path from Ti_2AlC to Ti_3AlC_2. *J. Am. Ceram. Soc.* **106**, 5567–5579 (2023).

38. Goossens, N. et al. Synthesis of MAX phase-based ceramics from early transition metal hydride powders. *J. Eur. Ceram. Soc.* **42**, 7389–7402 (2022).
39. Guan, K. et al. Efficient synthesis of Ti_3AlC_2 powders with high purity by microwave-assisted molten salt method. *Ceram. Int.* **48**, 16357–16363 (2022).
40. Xu, Y. et al. In situ grown two-dimensional TiO_2/Ti_3CN MXene heterojunction rich in Ti^{3+} species for highly efficient photoelectrocatalytic CO_2 reduction. *Chem. Eng. J.* **452**, 139392 (2023).
41. Chen, N. From high-yield Ti_3AlCN ceramics to high-quality Ti_3CNT_x MXenes through eliminating Al segregation. *Chin. Chem. Lett.* **31**, 1044–1048 (2020).
42. Zhang, K. et al. Cation-driven self-assembly of core–shell covalent organic frameworks@Ti_3CN MXene nanospheres for high-performance aqueous zinc-ion hybrid supercapacitors. *Chem. Eng. J.* **490**, 151369 (2024).
43. Zhou, S. et al. Vacancy-rich MXene-immobilized Ni single atoms as a high-performance electrocatalyst for the hydrazine oxidation reaction. *Adv. Mater.* **34**, 2204388 (2022).
44. Jiang, Y. et al. In situ turning defects of exfoliated Ti_3C_2 MXene into Fenton-like catalytic active sites. *Proc. Natl. Acad. Sci. USA* **120**, e2210211120 (2023).
45. Mao, C. et al. Photochemical acceleration of ammonia production by Pt_1–Pt_n–TiN reduction and N_2 activation. *J. Am. Chem. Soc.* **145**, 13134–13146 (2023).
46. Liang, L. et al. Multifunctional magnetic $Ti_3C_2T_x$ MXene/graphene aerogel with superior electromagnetic wave absorption performance. *ACS Nano* **15**, 6622–6632 (2021).
47. Zhong, X. et al. Heterostructured BN@Co-C@C endowing polyester composites excellent thermal conductivity and microwave absorption at C band. *Adv. Funct. Mater.* **34**, 2313544 (2024).
48. Wang, J. et al. Integration of heterogeneous interfaces and multi-dimensional encapsulation structure in Fe_2N@CNTs enabling highly efficient thermal management and microwave absorption. *Adv. Funct. Mater.* **34**, 2408696 (2024).
49. Fang, S. Self-assembled skin-like metamaterials for dual-band camouflage. *Sci. Adv.* **10**, eadl1896 (2024).
50. Sun, Y. et al. MoS_2-coated MOF-derived hollow heterostructures for electromagnetic wave absorption. *ACS Appl. Mater. Interfaces* **17**, 14278–14290 (2025).
51. Ma, X. et al. Co–Ni/C composite derived from N, S-codoped graphene decorate metal–organic framework toward microwave attenuation. *Langmuir* **41**, 3684–3694 (2025).
52. Yin, X. et al. 2D/1D hierarchical hollow NiO@PPy composites with tunable dielectric properties for enhanced electromagnetic wave absorption. *Small* **21**, 2408419 (2025).
53. Yang, X. et al. Confining magnetic response by the surface reorganization of buckling permalloy microspheres for boosting microwave absorption. *ACS Nano* **19**, 9144–9155 (2025).
54. Wu, T. et al. Hierarchical assembly of ternary MOF-derived sandwich composites for high-efficiency tunable electromagnetic wave absorption. *Small* **20**, 2407599 (2024).
55. Liu, Z. et al. Two-dimensional CNPs superstructures derived from metal–organic frameworks for electromagnetic wave absorption. *ACS Appl. Mater. Interfaces* **16**, 65173–65184 (2024).
56. Shi, Y. et al. High-coordination engineering of asymmetrical cerium single-atoms for advanced electromagnetic wave absorption. *Adv. Funct. Mater.* https://doi.org/10.1002/adfm.202504372 (2025).
57. Zeng, X. et al. Design of gel-based materials for electromagnetic wave absorption. *Adv. Funct. Mater.* **35**, 2502671 (2025).
58. Kresse, G. et al. From ultrasoft pseudopotentials to the projector augmented-wave method. *Phys. Rev. B* **59**, 1758–1775 (1999).
59. Perdew, J. et al. Generalized gradient approximation made simple. *Phys. Rev. B* **77**, 3865–3868 (1996).

Acknowledgements

This work was financially supported by the National Natural Science Foundation of China (grant nos. 52374305 and 51864030) (L.X.), the National Key R&D Program of China (nos. 2023YFA1507703) (L.X.), the Yunnan Fundamental Research Projects (nos. 202301AV070009 and nos. 202101AS070023) (L.X.), the China Petrochemical Corporation (Nos. 222038 and Nos. 223114) (L.X.), and by the Yunling Scholars Program for Xingdian Talent Support Plan (L.X.).

Author contributions

Experimentation: C.X., L.X., J.L., and Y.F. Data curation: C.X., L.X., and Z.S. Writing—original draft preparation: C.X. and L.X. Writing—review and editing: L.X. Methodology: C.X., L.X., Z.S., J.L., Z.H., and Y.F. Investigation: C.X., L.X., Z.S., Z.H., and Y.L. Conceptualization: C.X. and L.X. Support and supervision: L.X.

Competing interests

The authors declare no competing interests.

Additional information

Supplementary information The online version contains supplementary material available at https://doi.org/10.1038/s41467-025-63975-1.

Correspondence and requests for materials should be addressed to Lei Xu.

Peer review information *Nature Communications* thanks Chong Min Koo, and the other, anonymous, reviewer(s) for their contribution to the peer review of this work. A peer review file is available.